PAPER

Check for updates

New volumetric CNT-doped gelatin–cellulose scaffolds for skeletal muscle tissue engineering†

Ferran Velasco-Mallorquí,[a] Juan M. Fernández-Costa, [ID][a] Luisa Neves[b] and Javier Ramón-Azcón [ID] *[a]

Currently, the fabrication of scaffolds for engineered skeletal muscle tissues is unable to reach the millimeter size. The main drawbacks are the poor nutrient diffusion, lack of an internal structure to align the precursor cells, and poor mechanical and electric properties. Herein, we present a combination of gelatin-carboxymethyl cellulose materials polymerised by a cryogelation process that allowed us to reach scaffold fabrication up to millimeter size and solve the main problems related to the large size muscle tissue constructs. (1) By incorporating carbon nanotubes (CNT), we can improve the electrical properties of the scaffold, thereby enhancing tissue maturation when applying an electric pulse stimulus (EPS). (2) We have fabricated an anisotropic internal three-dimensional microarchitecture with good pore distribution and highly aligned morphology to enhance the cell alignment, cell fusion and myotube formation. With this set up, we were able to generate a fully functional skeletal muscle tissue using a combination of EPS and our doped-biocomposite scaffold and obtain a mature tissue on the millimeter scale. We also characterized the pore distribution, swelling, stiffness and conductivity of the scaffold. Moreover, we proved that the cells were viable and could fuse in three-dimensional (3D) functional myotubes throughout the scaffold. In conclusion, we fabricated a biocompatible and customizable scaffold for 3D cell culture suitable for a wide range of applications such as organ-on-a-chip, drug screening, transplantation and disease modelling.

Introduction

Nanomaterials have recently gained significant attention as tools to improve the electrical and mechanical properties of biomaterials.[1] For instance, alginate hydrogels impregnated with gold nanostructures improved the electrical conductivity and cellular excitability of both cardiomyocytes and neural cells.[2,3] Nanomaterials encapsulated in scaffold materials could also enhance the sensitivity of engineered tissues mimicking the native nervous system,[4] which can be used in fundamental cell biology and diagnostics. For example, carbon nanotubes (CNTs)[5] and nanowires[6] have been used to sense the extra- and intra-cellular activities of cells or to tailor the delivery of therapeutic molecules to cells.

The aim of tissue engineering is to fabricate, repair, and/or replace tissues and organs using cell technology, medicine, advanced materials, and engineering approaches.[7,8] Nanotechnology and microtechnology have made significant contributions to the field of tissue engineering in recent years. In particular, nanotechnology provides novel tissue engineering fabrication techniques and nano-composed biomaterials.

Scaffolds are the key part in the development of engineered tissues. They support the growth and differentiation of progenitor cells in 3D environments. Hydrogels are often used as scaffolds due to their high water content, biocompatibility, and biodegradability.[9,10] However, they generally have poor mechanical properties and low conductivity, which limit their application in regulating the behaviour of electroactive cells, such as skeletal, cardiac, and neural cells.[2] Therefore, controlling the mechanical and electrical properties of hydrogels is desirable in regulating cell behaviours. Electrically conductive and mechanically strong hydrogels have other important applications, such as the real-time monitoring of cellular activities[11,12] and developing hybrid three-dimensional (3D) electronics-tissue materials[13] and as bioactuators.[14]

To date, scaffolds for skeletal muscle tissue engineering have been generated mostly by the encapsulation of cells inside hydrogels,[15] both by bioprinting[16–18] or stamping[19,20] techniques. However, it is difficult to obtain a single hydrogel that meets all desirable properties. As mentioned above, these hydrogels are not conductive, and they lack optimal mechanical properties. *In vivo*, skeletal muscle cells are constantly triggered to contract by nerve signals that are transmitted to the muscle tissue through the neuromuscular junctions.[21,22] Without these nerve signals,

[a]Institute for Bioengineering of Catalonia (IBEC), The Barcelona Institute of Science and Technology (BIST), Baldiri I Reixac, 10-12, Barcelona, Spain. E-mail: jramon@ibecbarcelona.eu

[b]Multiwave Imaging, Hotel Technoptic, 2 Rue Marc Donadille, 13013 Marseille, France

muscle development is impaired. Therefore, controlling the mechanical and electrical properties of hydrogels is desirable to facilitate the regulation of muscle cell behaviours (Fig. 1a). The positioning of cells, delivery of molecules, and design of scaffolds from the nanoscopic scale to the macroscopic scale can be achieved using novel nanotechnologies.[7,23–27] In order to enhance the electrical properties of the scaffolds, some approaches have integrated nanoparticles as graphene,[28] gold,[29] silver,[30] iron oxide[31] or CNTs.[32,33] However, these fabrication approaches cannot be scaled up to engineer scaffolds in the centimeter or millimeter range, because the porosity is small and the low nutrient diffusion makes them inadequate for long-term cell culture. Another issue is the pre-alignment of cells to obtain long and functional differentiated tissues. To overcome these limitations and in order to generate a bigger 3D functional aligned muscle tissue, the cryogel approach technology has been proposed in this work. This technique allows the generation of a millimeter range scaffold, with high pore interconnectivity and a better mechanical stability than the hydrogel-based scaffolds for generating skeletal muscle tissue by mimicking its 3D environment.

Cryogels are microporous scaffolds[34–36] with a pore range from a few micrometers up to hundreds of micrometers. The pores are a consequence of water ice crystallization after freezing the polymer solution (Fig. 1b). Once the cryogel is thawed, the ice crystals leave behind empty pores. We were able to modulate the pore morphology by applying different freezing directionalities.[37,38] As the skeletal muscle needs a highly aligned morphology to enhance its alignment and fusion, we generated an anisotropic morphology by forcing the directionality of the freezing from one single axis. In that way, the ice crystallization allowed us to fabricate a mechanically stable scaffold for skeletal muscle tissue engineering.

Here, we present a new gelatin–microcellulose biomaterial composite (Fig. 2) doped with CNTs with mechanical stability, anisotropic pore morphology and electrical properties applied in skeletal muscle tissue engineering. We have fabricated a scaffold based on the combination of a natural degradable biomaterial with a non-biodegradable material by mammalian cells using gelatin and carboxymethyl cellulose. Gelatin has good properties for tissue regeneration, such as pore structure, permeability, and hydrophilicity, with natural cell binding motifs, such as the tripeptide Arg-Gly-Asp (RGD) and it is stable *in vivo*.[37,39] However, to improve its mechanical stability, the incorporation of carboxymethyl cellulose (CMC) has been proposed. CMC is a linear, long-chain, water-soluble, anionic polysaccharide that is taken from the cellulose and can be degraded by non-mammalian cells.[40] This new doped bio-composite has an anisotropic pore distribution, high fiber alignment and good pore diameter that allow for highly efficient nutrient diffusion. The formation of nanofiber web-like structures of CNTs within hydrogels resulted in hybrid hydrogels with enhanced mechanical properties compared with the unmodified hydrogels. An anisotropic conductive scaffold is highly beneficial for the fabrication of functional skeletal muscle tissue constructs with the aid of electrical stimulation. All of these features combined with the technique of cryogelation allow us to generate millimeter-range scaffolds. In this work, we demonstrated that myoblasts could be aligned following this pore structure, colonizing the whole 3D structure,
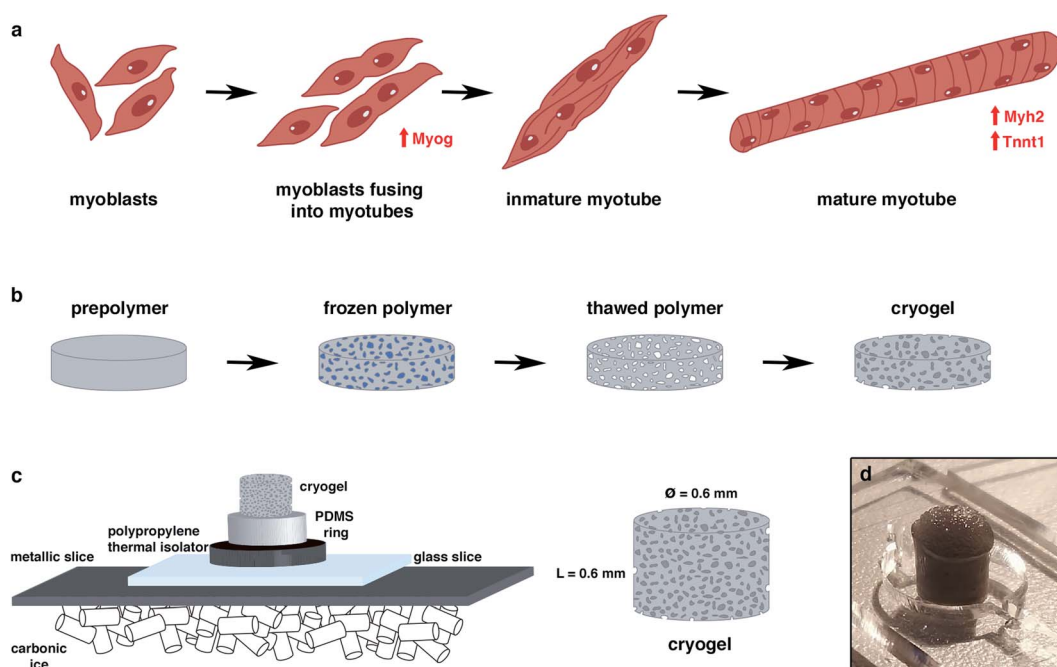

Fig. 1 General overview of the study. (a) Myogenic differentiation process. Muscle precursor cells and myoblasts were fused to form immature myotubes, while the myogenin (Myog) expression increased. Myotube maturation implied an upregulation of Myosin Heavy Chain 2 (Myh2) and tropomyosin (Tnnt1) genes. (b) Principle of the cryogelation technique. (c) Protocol to generate a highly anisotropic cryogel.
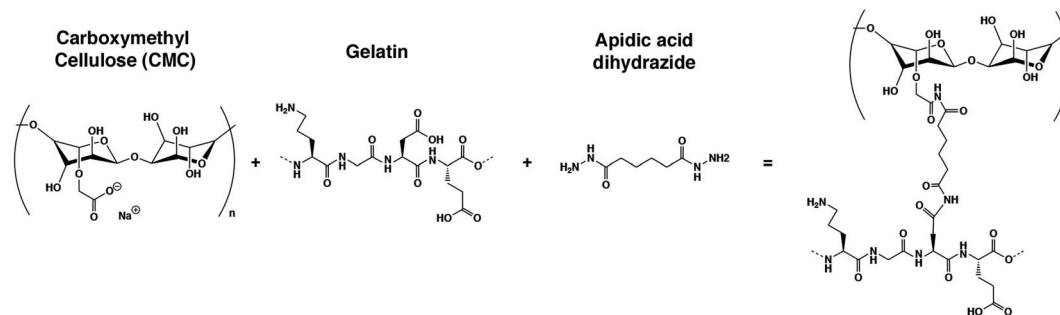
Fig. 2 Chemical structure of the reagents and final structure after crosslinking.

and fusing into myotubes. We also proved that the electrical stimulation, in combination with this scaffold, enhances the maturation of these cells. All of these features make this new CNT-doped gelatin-CMC biomaterial composite a promising scaffold to engineer millimeter-range skeletal muscle tissue for many applications.

Experimental procedures

Cryogel fabrication

To fabricate carboxymethyl cellulose (Sigma Aldrich) at 1% (w/v), gelatin from porcine skin (Sigma Aldrich) and 2% (w/v) cryogels were dissolved into Milli-Q water under stirring conditions. Once the CMC and gelatin were dissolved, the crosslinking reagents were prepared. Adipic acid dihydrazide (AAD, Sigma Aldrich) at 50 mg mL^{-1}, MES buffer from MES hydrate (Sigma Aldrich) at 0.5 M and pH at 5.5 and N-(3-dimethylaminopropyl)-N'-ethylcarbodiimide hydrochloride (EDC, Sigma Aldrich) at 1 mg μL^{-1} all dissolved in Milli-Q water and were vortexed to ensure homogeneity throughout the solution. To fabricate the prepolymer solution, 0.5 mL of CMC was mixed with 0.5 mL of gelatin, 100 μL of MES buffer, 100 μL of Milli-Q water, 21 μL of AAD and 4 μL of EDC. The mixture was then vigorously pipetted to avoid early crosslinking before freezing. For the stained cryogels, 12 μL of 1 mM fluoresceinamine (Sigma Aldrich) was added to the prepolymer solution. In the case of the doped cryogels with carbon nanotubes, 100 μL of CNT (Sigma Aldrich) at 2 mg mL^{-1} dissolved in Milli-Q water was added in substitution of the 100 μL of Milli-Q water. Then, the molds, which consisted of a circular pool of PDMS (5 mm height × 6 mm diameter) surrounded by a polypropylene thermal isolator and a square cover glass (24 × 24 mm^2) on the top, were filled with the final prepolymer solution. Once filled, the mold was quickly placed over a metallic sheet above carbonic ice and allowed to freeze for 1 hour (Fig. 1c). Then, the molds were placed into a −20 °C freezer for 24 hours. The next day, the crosslinked cryogels (Fig. 2) were removed carefully from the cover glass and PDMS mold, and subsequently cut. For the 3D approach, the top and bottom parts were cut to avoid the regions with small porosity. After slicing the cryogels, they were submerged in cleaning solution for 5 minute consecutive cleaning steps. The cleaning solution was composed of 1× Milli-Q water, 1 × 100 mM NaOH (Panreac), 1 × 10 mM EDTA (Sigma

Aldrich), 1× MilliQ and 3× PBS (Sigma Aldrich). Once the cleaning protocol was finished, the cryogels were sterilized in an autoclave for further cell seeding experiments.

Mechanical and electrical properties of the GelMA-CMC and GelMA-CMC-CNTs cryogels

Pore analysis. For the pore analysis, we used stained cryogels. Once autoclaved, the z-stack images were examined with a confocal microscope. The different pore diameters were quantified with ImageJ software. We analyzed 20 different images per cryogel, with 20 μm of distance in the z-axis between the images, and 3 cryogels. For the diameter quantification, the minFeret approximation was used in order to calculate the small diameter of each pore. The small diameter was used as the minimal distance of the pore, so it was a good indication to see if the cells could infiltrate the cryogel.

The cryogels were fabricated for the SEM images. After sterilizing, ethanol dehydration was done to substitute the water for ethanol. Starting at 50% ethanol, consecutive washings were done by increasing the percentage of ethanol up to 70%, 80%, 90%, 96% (×2) and 99.5% ethanol. Once all of the water was substituted with ethanol, a critical point dry was done in order to remove all the ethanol and replace it with CO$_2$. Then, carbon sputtering was performed, and the SEM images were taken using a JEOL JSM-7001F at 10 kV.

Conductivity. To measure the dielectric properties of the samples, a tapered transmission line method was used. The conical feature of the cell allows the insertion of a watertight sample-holder (SH), providing a significant increase of the net sample volume. This modification permitted the evolution of the coaxial line in terms of the types of materials measured,[41,42] in addition to the speed and flow of acquisition.[43]

In this study, the cell was connected to a calibrated Anritsu MS46122B VNA, which enabled the extraction of the S-parameters S_{11}, S_{12}, S_{21}, and S_{22} of the cell and sample. Knowing the intrinsic electric distances between the connectors and sample, and considering the attenuation of the cell, it is possible to carry out a de-embedding process, where the S-parameters of the sample are extracted through the S-parameters of the cell and sample.

The acquisition method of the complex permittivity is based on the Nicolson–Ross[44] & Weir[45] algorithm. Through the sample

S-parameters, it is possible to determine the reflection (Γ) and transmission (T) coefficient, as seen in eqn (1)–(6),

$$\Gamma = \frac{1 + S_{11}^2 - S_{21}^2}{2S_{11}} \pm \sqrt{\left(\frac{1 + S_{11}^2 - S_{21}^2}{2S_{11}}\right)^2 - 1} \qquad (1)$$

$$T = \frac{S_{11} + S_{21} - \Gamma}{1 - (S_{11} + S_{21})\Gamma} \qquad (2)$$

$$z_r = \left(\frac{1 + \Gamma}{1 - \Gamma}\right) \qquad (3)$$

where z_r is the reduced impedance of the system. A condition that must be respected at this point is that the magnitude of $|\Gamma|$ must be equal or inferior to the unit. Thus, it is possible to determine the complex permittivity (ε^*), the complex permeability (μ^*), and the conductivity (σ), expressed in S m^{-1}.

$$\mu_r = j\frac{c}{2\pi fL}\left(\frac{1 + \Gamma}{1 - \Gamma}\right)\ln\left(\frac{1}{T}\right) \qquad (4)$$

$$\varepsilon_r = j\frac{c}{2\pi fL}\left(\frac{1 - \Gamma}{1 + \Gamma}\right)\ln\left(\frac{1}{T}\right) \qquad (5)$$

$$\sigma = 2\pi f \varepsilon'' \varepsilon_0 \qquad (6)$$

Here, L represents the sample length, c is the speed of light in a vacuum, and ε_0 is the permittivity of the free space, 8.85×10^{-12} F m^{-1}.

An SH of length 6 mm was used to measure the samples from 10 MHz to 8 GHz, at room temperature (RT) conditions (26.8 °C, 31% humidity).

The cylindrical samples have a similar diameter and length as the SH, so the samples were simply introduced into the SH. In this configuration, the CNTs were aligned with the axis of the cell.

Swelling. Swelling is the water uptake capability of a biomaterial. In order to measure this capability, cryogels were fabricated as explained previously, sterilized, dried at RT and weighed. Next, the cryogels were submerged into Milli-Q water for up to 5 days when they reached equilibrium, and weighed again. The swelling ratio was calculated as follows:

$$\text{Swelling ratio} = \frac{W_{eq} - W_d}{W_{eq}} \times 100$$

where W_{eq} is the weight in equilibrium and W_d is the dry weight. 3 cryogels per condition were measured in this assay.

Stiffness. Compression assays were performed to determine the stiffness of our samples. The compression was applied both in the x- and y-axis in order to check the correct anisotropy of the cryogels. Biaxial compression assays were performed in a Zwick Z0.5 TN instrument (Zwick-Roell) with 5 N load cell. The experiment was performed with samples at room temperature at up to 30% of the final compression range at 0.1 mN of the preloading force, and at 20%/minute of the strain rate. Finally, the Young modulus was calculated from the slope of the range from 10% to 20% of the final compression. In these experiments, we tested 3 measurements per cryogel and axis and 3 cryogels per condition.

Culture of C2C12 myoblasts in the GelMA-CMC and GelMA-CMC-CNTs cryogels

Cell culture. The C2C12 myoblasts (American Type Culture Collection (ATCC)) were cultured in growth medium (DMEM, high glucose with L-glutamine (Gibco, Thermofisher) supplemented with 10% FBS (Thermofisher) and 1% Pen/Strep (Thermofisher)). When 70–80% confluence was reached, the C2C12 myoblasts were trypsinized using 0.25% trypsin/0.1% EDTA and subsequently plated in a 1 : 4 density ratio. The cells were maintained in a cell culture incubator (Sanyo) with a 5% CO$_2$ atmosphere at 37 °C.

C2C12 seeding into the cryogel. First, the cryogel pores were kept dry for 30 minutes at RT. For cell seeding, a concentration of 9×10^6 cells per mL was used. Upon achieving this concentration, a drop of 20 μL was seeded into the upper part of the cryogel. After 10 minutes, we collected the medium from the bottom that could pass through the cryogel, and we reseeded it at the top of the cryogel again. After cell inoculation, the cryogels were in the growth medium for 10 days, and then the medium was changed to a differentiation medium (DMEM high glucose with L-glutamine (Thermofisher) supplemented with 2% horse serum (Thermofisher) and 1% Pen/Strep (Thermofisher)) for up to 22 days of culture in order to promote myotube formation.

Immunostaining protocol. For confocal analysis, stained cryogels were used. After culturing the cells, the cryogels were washed with PBS and fixed with a 10% formalin solution (Sigma Aldrich) for 30 minutes. Then, the cryogels were washed with Tris Buffered Saline (TBS, Canvax Biotech) and permeabilized with 0.1% v/v Triton X-100 (Sigma Aldrich) solution in TBS for 15 minutes. Following this procedure, the blocking of the cryogels was done with a blocking solution of 0.3% v/v Triton X-100 and 3% v/v Donkey serum (Sigma-Aldrich) in TBS for 2 hours. Then, 100 nM Rhodamine-Phalloidin 480 (Cytoskeleton Inc) and 5 μg mL^{-1} MF20 Alexa Fluor 488 (eBioscience) in blocking solution was incubated overnight at 4 °C. Rhodamine-Phalloidin 480 was used for F-actin and MF20 Alexa Fluor 488 for Myosin Heavy Chain (red and green staining, respectively). The following day, the cryogels were washed with permeabilization solution (3×, 10 minutes each). Subsequently, the cryogels were incubated with 1 μM DAPI (Thermofisher) for nuclei counterstain into the blocking solution for 15 minutes. Finally, the cryogels were washed with TBS for 15 minutes and stored at 4 °C until acquired for confocal microscopy. Images were taken using a LSM 800 confocal microscope from Zeiss.

Viability assay. Viability assays were performed using the Live/Dead assay kit (Thermofisher), in accordance with the manufacturer's instructions. The assays were performed at days 1, 5 and 7 of culture after seeding in both types of cryogels with or without CNTs. Briefly, the cryogels were washed for 5 minutes with PBS (Phosphate Buffered Saline, 0.01 M phosphate buffer, 0.0027 M potassium chloride and 0.137 M sodium chloride, pH 7.4, Sigma-Aldrich) five times to replace the culture medium, and subsequently incubated with the final dye solution. This solution consisted of 12 μL of 12 mM EthD-1, 3 μL of 4 mM calcein AM and 6 μL of Hoechst for the dead cells, live cells and

nuclei, respectively, into 6 mL of PBS. Then, the solution was vortexed, and 2 mL of this solution was added to each cryogel and incubated for 25 min at 37 °C. Then, the cryogels were washed 3 times with PBS. Finally, confocal images were taken using a Zeiss LSM 800 confocal microscope. The quantification of the live/dead ratio was calculated using ImageJ software, and was determined as follows:

$$\text{Live ratio} = \frac{\#\text{Nuclei} - \#(\text{Nuclei} - \text{EthD areas})}{\#\text{Nuclei}} \times 100$$

Cell alignment. To calculate the alignment of the fibers, fluorescein-stained cryogels were used. In addition, nuclei and F-actin for the cells were stained following the immunostaining protocol. Confocal images were obtained using a Zeiss LSM 800 confocal microscope. For this quantification, 5 images per cryogel were taken. The ImageJ PlugIn "OrientationJ" software was used to see the distribution of the aligned fibers and the alignment of the cells in a random fiber distribution of the cryogel against the anisotropic cryogels.

Electrical stimulation. An electric pulse stimulation (EPS) was applied at day 11 after induction of the myogenic differentiation. The stimulation was performed by placing the cryogels inside a 6-well plate C-dish from IonOptix connected to a multifunction generator (WF 1948; NF Co.) with a specified regime (1 Hz of frequency, 1 V p–p and 10 ms of width) for 12 consecutive hours.

Fusion index. For differentiation of the myoblast into myotubes, the cells were seeded as previously explained in the cryogel and cultivated for 22 days. For those that were stimulated, EPS was applied to the cryogels at day 21 of culture. Cryogels were inmunostained as described above, and sliced vertically to improve the image acquisition. Then, the confocal images were taken at 5 random areas over the cryogel, and 3 cryogels per condition were used. From these images, the fusion index was calculated. The index fusion consisted of the number of cells that were differentiated and fused. To calculate the fusion index, the following equation was used:

$$\text{Fusion index} = \frac{\#\text{Green \& blue areas}}{\text{Total }\#\text{nuclei}} \times 100$$

For the index fusion analysis, 5 images per sample and 3 samples per condition were taken and analysed.

RNA isolation, retrotranscription and real-time quantitative polymerase chain reaction (qRT-PCR)

For the total RNA isolation of the single cryogels, a standard organic extraction using TriReagent (Sigma) was performed. Briefly, single cryogels were homogenized with 1 mL of TriReagent at room temperature and mixed with 200 μL of chloroform. Samples were centrifuged at 12 000 rcf for 15 minutes at 4 °C and the aqueous phase was collected. Finally, RNA was precipitated using isopropanol and GlycoBlue (Invitrogen) as the carrier. One microgram of total RNA was digested with DNAse I (Invitrogen), and retrotranscribed with SuperScriptII

(Invitrogen) using random hexanucleotides. For each biological replicate, qRT-PCR reactions from 10 ng of cDNA were carried out per triplicate using HOT FIREPol EvaGreen qPCR Mix Plus (SolisBiodyne). The primers used were: 5′-CATTGCTGA-CAGGATGCAGAAGG-3′/5′-TGCTGGAAGGTGGACAGTGAGG-3′ for ActB, 5′-GCTGGAAGATGAGTGCTCAGAG-3′/5′-TCCAAAC-CAGCCATCTCCTCTG-3′ for Myog, 5′-GCGACTTGAAGTTAGCC-CAGGA-3′/5′-CTCGTCCTCAATCTTGCTCTGC-3′ for Myh2 and 5′-GAGCAGAGGATGACGCCAAGAA-3′/5′-TTCATCTCCCGAC-CAGTCTGTC-3′ for Tnnt1. Expression levels were measured using an Applied Biosystems StepOnePlus Real Time PCR System. The expression level relative to the ActB endogenous genes and the control group was calculated using the $2^{-\Delta\Delta C_t}$ method. Pairs of samples were compared using the two-tailed t tests ($\alpha = 0.05$), applying Welch's correction when necessary. The statistical differences were estimated by the Student's t tests ($p < 0.05$) on normalized data. At least three cryogels per condition were evaluated.

Statistical analysis. For pore analysis, we analysed 20 different images per cryogel, with 20 μm of distance in the z-axis between images, and 3 cryogels. For swelling, 3 cryogels per condition were assessed. This was performed similarly for the stiffness, where we tested 3 measurements per cryogel and axis, and 3 cryogels per condition. In the case of the alignment image quantification, 3 samples per condition and 5 images per sample were taken and evaluated. For the viability and fusion index analysis, 3 cryogels per condition and 20 images per sample were taken and evaluated. For the qPCR, 2 different experiments were done. In each experiment, 3 cryogels per condition and 2 replicas per sample were performed. For statistical analysis, the two-tailed Student t-test ($\alpha = 0.05$) was used to check the statistical significance of all samples.

Results and discussion

Cryogel fabrication and mechanical characterization

The protocol to fabricate cryogels (Fig. 1c) was taken and modified from a previous study.[36] The size of the scaffold (6 mm of diameter × 6 mm of height) was chosen as a good area for seeding in the x-axis and a good length in the y-axis. This was enough to form the desired anisotropic structure. 2% gelatin – 1% CMC (w/v) cryogels (Fig. 2) was chosen as the ideal one. This was because it is the lowest possible material concentration with enough stiffness to hold and handle the scaffold without breaking it. In addition, results not shown in this study proved that as the material concentration was decreased, a bigger pore size could be achieved.[37] According to the approach used, big tubular pores were expected to facilitate the cell seeding and migration through the cryogel. We have obtained volumetric constructions in the range of millimeters. Previous scaffolds made by encapsulation into hydrogels could not reach these dimensions due to their low mechanical properties or pore distribution, leading to a lack of nutrient diffusion. As we have shown in previous works, when the cells are encapsulated in depths of more than 200 μm, their viability decreases.[46] The pore sizes of most hydrogels described to date are small. This characteristic feature in the hydrogels leads to difficulties in

nutrient diffusion. This is the main reason why bioprinted hydrogels have dimensions that are smaller than 500 μm.[21,47,48] However, using our unidirectional cryogelation technique, we obtained cryogels with enough pore size and high-water retention capability to allow for fast nutrient and medium diffusion along the entire scaffold. Specifically, our cryogel has a flow rate of 0.034 mL min^{-1}.

By analyzing the pore distribution, we can observe that small pores are always present (Fig. 3a and b). However, most of the pores are in a specific range between 30 and 75 μm of the diameter. This pore range is appropriate for seeding the cells over the cryogel. Moreover, this pore size range allowed for cell growth and migration, and finally colonization throughout the whole cryogel. Myotube maturation implied the alignment and fusion of myoblast precursors. The mature myotubes had a dimension that was not larger than 30 μm in width,[49,50] so the pore size of our cryogels would allow for the correct myotube maturation. Supporting the pore distribution analysis, the scanning electron microscope images showed this same distribution, where most of the pores were bigger than 30 μm diameter (Fig. 3a). In addition, we can appreciate the tubular shape of these pores. The vertical cross-section of the fluorescein-stained cryogels taken with a confocal microscope proved that the anisotropy of the fibers was achieved (Fig. 3c). This feature is a highly important feature for engineering the skeletal muscle tissue, as the skeletal muscle tissue needs high alignment and superorganization to differentiate between the

myoblasts and myotubes. With the technique, we achieved a good pore distribution and pore size that allowed for a good infiltration of the cells. Moreover, the cryogel pores had a high alignment that enhanced the fusion and differentiation of the skeletal muscle myotubes. Although there are other techniques to achieve this alignment to enhance cell fusion, such as bioprinting,[46] stamping[48,51] or stretching,[52] our technique allowed us to enhance this alignment using surface directionality, as some 2D approaches used to generate this alignment without encapsulating.[52–55] Combining 3D directionality plus millimeter size, we were able to obtain volumetric tissue constructions. By combining these features with our technique, we could obtain a good scaffold to engineer highly organized tissue as skeletal muscle. Cryogelation showed a strong and nonharmful technique for generating the scaffolds with a higher pore distribution, synonymous with a higher nutrient diffusion and low confinement of the cells. This implied less difficulties in the proliferation and migration.

Electric stimulation improves *in vitro* myotube maturation.[56] Unfortunately, most of the scaffolds used for tissue engineering have low conductivity. Therefore, this electrical stimulation to myogenic maturation is not very effective. In order to increase the conductivity of our scaffolds, we incorporated carbon nanotubes (CNTs) to our cryogels. In order to do this, we incorporated the CNTs mixed in the prepolymer solution. By doing so, when all of the process of crosslinking happens, the CNTs stay in the fiber network. Analysis of CNTs distribution by bright field microscopy showed that the incorporation of CNTs was not homogeneous (Fig. 3d). The CNTs formed aligned aggregates through the cryogel. To test if the CNTs improved the electric properties of the cryogels, we performed conductivity assays (Fig. 4a). This conductivity was similar in the low frequency ranges. From 1×10^7 to 2.5×10^8 Hz, the conductivity was around 1 S m^{-1} for cryogels both without and with CNTs. However, the conductivity of the CNT cryogels increased faster with frequency than the ones without CNT. Moreover, CNTs increased the conductivity of the cryogels at higher frequencies up until 2×10^9 Hz, where the cryogels with CNTs reached 5.71 S m^{-1} *vs.* 4.08 S m^{-1} for the cryogels without CNTs (Fig. 4b). The conductivity achieved with our scaffolds was similar to or higher than other scaffolds used for the maturation of myotubes.[57,58] In previous electrically stimulated scaffolds for skeletal muscle tissue engineering studies, conductivities from 10 mS m^{-1} to 6.4 S m^{-1} were achieved, and maturation of the tissue was enhanced. In our case, we could enhance the electrical properties of the scaffold. In addition, we were able to modulate the frequency and conductivity of these scaffolds. In this way, we can obtain different conductive values, but always in the range of previous studies. Notably, the conductivity can be modulated by changing the concentration of CNT.[59] However, there is a big disparity in the literature about the ideal conductivity of a scaffold to engineer and enhance myogenic differentiation. This disparity gives a real advantage for our scaffold, as we are able to modulate the conductivity. The high conductivity of our cryogels makes them suitable for many EPS (Electrical Pulse Stimulation) assays for the maturation or even contraction of the skeletal muscle tissue.
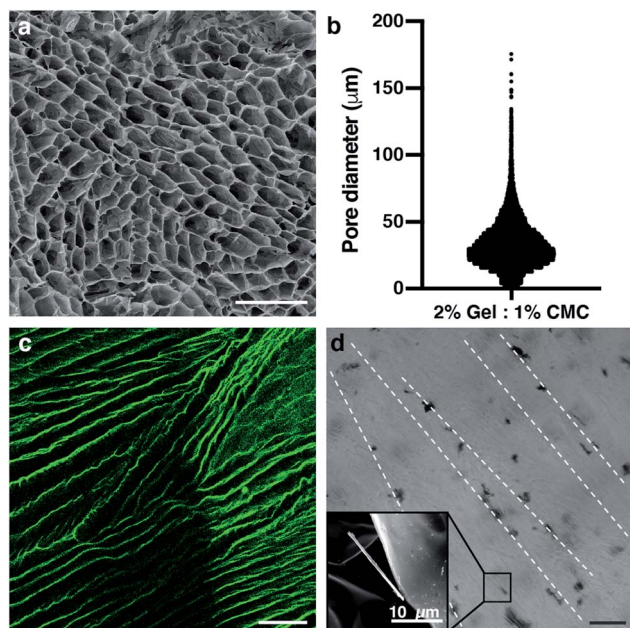

Fig. 3 The pore size distribution and tubular pore morphology among the scaffold fit with the skeletal muscle tissue engineering needs. (a) Scanning electron microscope (SEM) image of the pores of the cryogel. (b) Diameter distribution of the pores among the 2% gelatin – 1% CMC cryogel. (c) Confocal image of the cryogel anisotropic fibers marked with aminofluorescein in green. (d) Bright field image of the CNT distribution inside the cryogel. SEM image of a CNT is shown in the small inset. Scale bars = 100 μm.
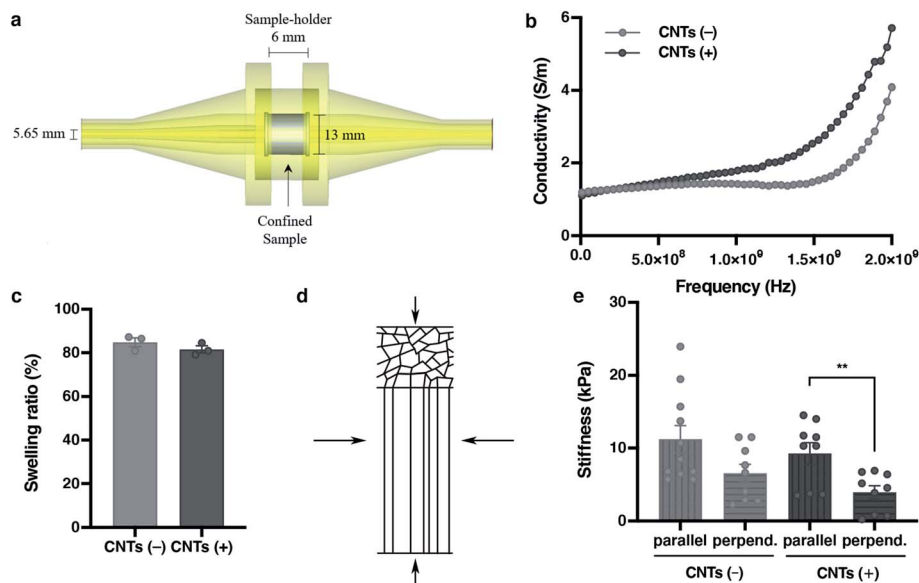
Fig. 4 Mechanical characterization of the scaffold sets. Its features are the ideal ones for generating skeletal muscle tissue. (a) The conical coaxial adjustment of the EpsiMu transmission line. (b) Conductivity (S m^{-1}) of the cryogels. (c) Swelling ratio of each cryogel. (d) Compression axis from the stiffness assay of the cryogel. Vertical arrows are the parallel condition and horizontal arrows are the perpendicular condition. (e) Stiffness results for cryogels in both directions. (b, c and e) CNTs(−) in light grey and CNTs(+) in dark grey. All results are mean ± SEM. *p-value = 0.05.

Nutrient diffusion is an important feature for scaffolds in tissue engineering, and even more so for big volumetric scaffolds. To estimate the nutrient diffusion in our cryogels, we analysed the swelling ratio. The swelling ratio is the water uptake capability of a scaffold. Several features of the scaffold could affect the swelling ratio. We observed that the main factor is the amount of material. Also, we observed that the pore morphology had an effect in the swelling ratio (data not shown). A lower material concentration implies a higher pore distribution. In addition, a higher pore distribution implies more capability for the cryogel to take up water and more nutrient diffusion. The analyses of the swelling show that our cryogels have a high swelling ratio (84.81 ± 3.52%), indicating that the cryogels have not only a good porosity, but also a good interconnectivity. This would lead to a high nutrient diffusion. Notably, the addition of CNTs into the cryogels did not affect the swelling characteristic of the cryogel (84.81 ± 3.52% for CNTs(−) vs. 81.58 ± 2.78% for CNTs(+)) (Fig. 4c).

In addition, every tissue has its own characteristic environment. For this reason, the resemblance with the in vivo ECM is a highly important feature for the proper tissue formation. To generate a scaffold that mimics the physiological environment, stiffness is another important property to consider in designing good scaffolds for tissue engineering. As cells behave differently when the scaffold stiffness changes,[51,60] it is fundamental to have a scaffold that most closely resembles the in vivo condition for tissue engineering. To analyse the stiffness of the cryogels, a compression assay was performed. The Young's modulus was calculated from the linear part of the stress–strain curves, and measurements from two different axes were made to prove the anisotropy structure of the cryogel. As expected, the stiffness changed due to the fiber anisotropy when the compression was

applied perpendicularly or parallel to the fibers (Fig. 4d). This tendency of the values proved that the stiffness changed, depending on the directionality of the applied compression (11.21 ± 6.11 kPa for parallel/CNTs(−) vs. 6.52 ± 3.75 kPa for perpendicular/CNTs(−)) against the fibers (Fig. 4e). When the compression was applied along the perpendicular axis, there were some empty spaces from the pores that allowed the cryogel to compress. On the other hand, when the compression was applied in the parallel direction, it was harder to compress the fibers due to its alignment. In addition, as with the swelling properties, the addition of the carbon nanotubes did not affect the stiffness along any of the axes (9.24 ± 4.46 kPa for parallel/CNTs(+) vs. 11.21 ± 6.22 kPa for parallel/CNTs(−), and 3.90 ± 2.7 kPa for perpendicular/CNTs(+) vs. 6.52 ± 3.75 kPa for perpendicular/CNTs(−)). Remarkably, the stiffness of the cryogel showed in vivo similarity mechanical properties[51,61] at around 12 kPa stiffness, while the traditional hydrogels with the same amount of material had less in vivo resemblance.[46,62] Of importance, our results suggest that the addition of CNTs did not change the mechanical features of the scaffolds. So, we can improve the conductivity without losing any important feature of the scaffold. The combination of all of these features is a good point for engineering electrically stimulated tissues, such as skeletal muscle.

CNT-doped cryogels allow cell alignment and viability for long term cultures

C2C12 cells (mouse skeletal muscle immortalized myoblasts) were seeded inside the cryogel by gravity, as they cannot be encapsulated like hydrogels. To be able to form tissue without cell encapsulation is another important point to consider. Normally, encapsulation of the cells inside hydrogels implies
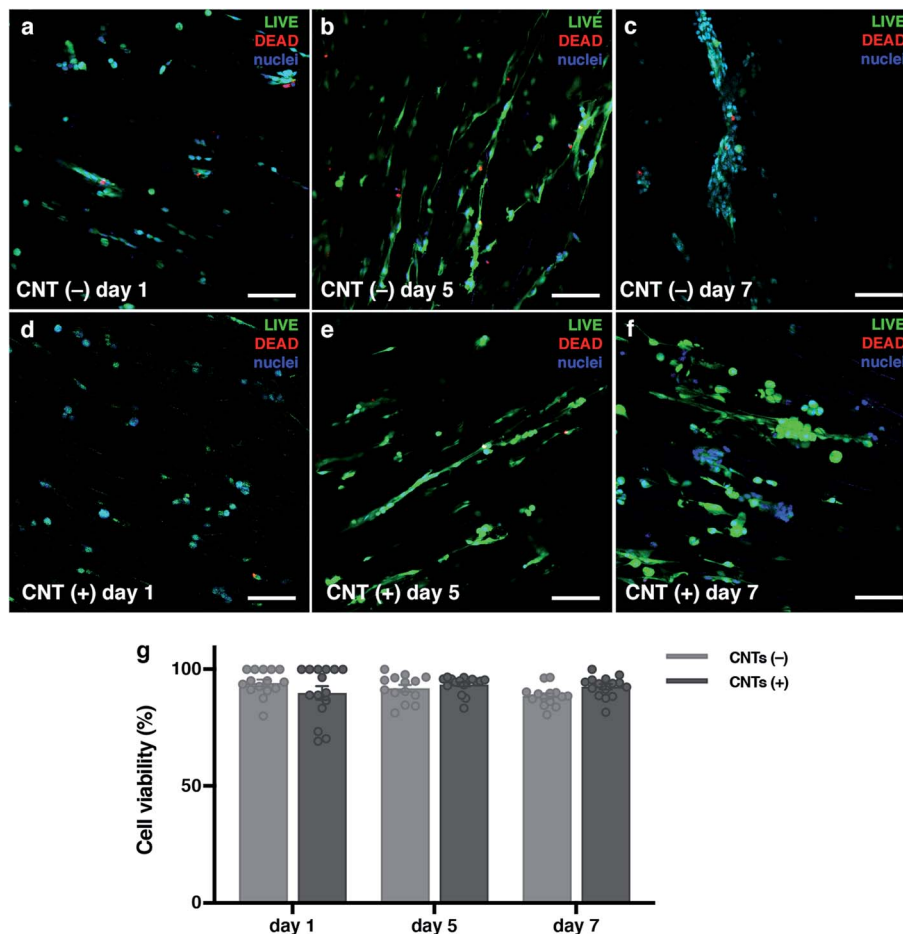
Fig. 5 Cells are viable when seeded inside the cryogel. (a–f) Confocal merged images of Live/Dead assay on different days. Live cells are marked in green with calcein AM, dead cells are marked in red with EthD-1, and cell nuclei are counterstained in blue with DAPI. (g) Graphs of the viability results. CNTs(−) in light grey and CNTs(+) in dark grey. Results are mean ± SEM. *p-value = 0.05.

the polymerization of the matrix using external crosslinkers like UV light, chemical reagents or temperature changes. This exposition to different crosslinkers could damage these cells. The cryogelation technique can solve this main drawback, as the scaffold polymerization occurs before seeding. An important point for engineering skeletal muscle is the cell density for seeding into the scaffold, as myoblasts need to be confluent in order to fuse into myotubes. We optimized the cells density at 9×10^6 cells per mL to allow for proliferation and colonization throughout the biomaterial. Other models for engineering the skeletal muscle tissue use similar or higher densities.[19,63] Nevertheless, at higher concentration, the cells did not properly colonize our cryogel because they formed a layer on the top (data not shown). After seeding, cells were cultured for 10 days in growth medium to promote cell proliferation and scaffold colonization. Then, the medium was replaced to differentiation media to promote myotube formation for 12 additional days. By immunostaining and confocal microscopy analysis, we could prove that the cells were found throughout the scaffold and they were distributed homogenously through the cryogel, demonstrating that the cells could colonize the entire depth of the cryogel (Fig SI1†).

To determine if the CNT-doped cryogel could be toxic for the cells, we decided to analyse the viability of the cells and if they could proliferate in the first few days. A Live/Dead assay was performed, and we determined that the viability of the C2C12 cells was always higher than 88%. In addition, there was no statistical significance between any day and condition (Fig. 5). However, an increase of the dead cells could be seen throughout the entire experiment. As the cells also proliferated, this ratio did not increase statistically. These high viability results are due to the crosslinking technique that allow us to seed the cells without suffering any damage due to the crosslinking process. The pore size and high pore distribution, which led to a high nutrient diffusion, also positively affected the high cell viability. More importantly, as reported previously, the CNT had no toxic effect.[64,65] The results compared on the same day with and without CNT were non-statistically significant, meaning there was also a good viability in the CNT scaffolds.

As mentioned, another important feature for engineering skeletal muscle is the cell alignment to enhance myogenic maturation. For this reason, one of the properties we wanted for our scaffold is the high anisotropy of the pores to promote cell alignment and fusion. Comparing the random pore
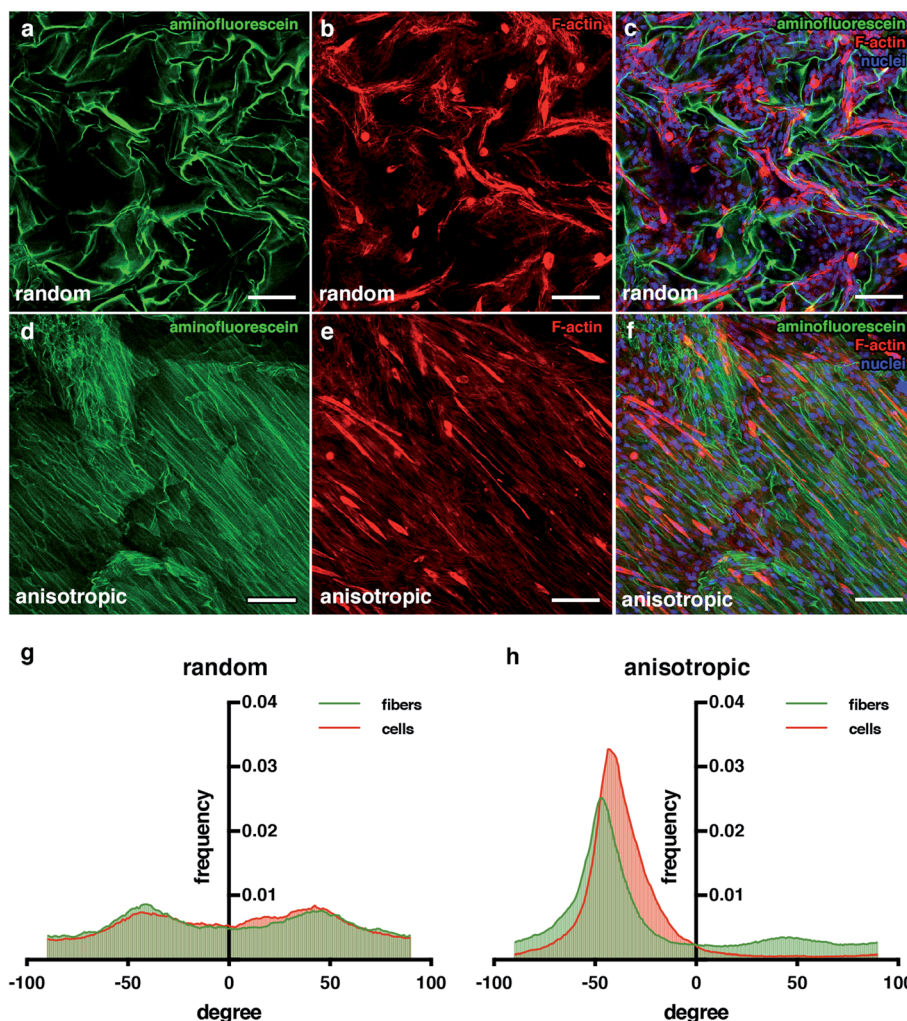
Fig. 6 Anisotropic cryogels improve cell alignment. (a–f) Confocal microscopy images showing an aminofluorescein-marked cryogel in green (a and d), cells marked with phalloidin in red (b and e) and cell nuclei counterstained in blue with DAPI. (c and f) Images showing merged channels. Scale bars = 100 μm. (g and h) Quantification of fibers and cell orientation. Graphs show frequency of fibers in each orientation degree.

morphology *versus* the anisotropic pore morphology (Fig. 6), we can appreciate that the cells in the anisotropic aligned much more clearly that the random one. Analysis with the ImageJ software demonstrated that the distribution obtained for the random pore distribution had more variability among all angles compared with the anisotropic structure one. In addition, it can be appreciated that in both pore morphologies, the alignment distributions for the cryogel fibers and cells were very similar (Fig. 6b). These results indicate that the cells sensed the pore morphology, and they could distribute and align following the morphology of the pores. The alignment of the cells was proved by the enhancement of their fusion;[50,66] thus, these results indicate that our cryogels could improve the myogenic maturation.

Electric stimulation of C2C12 cultured in CNT-doped cryogels enhances myoblasts fusion and myogenic maturation

Electrical Pulse Stimulation (EPS) was applied to prove that this new electrically improved composite enhanced the myogenic

maturation of the C2C12 myoblasts. To check the myotube formation, we analysed the expression of the muscle maturation marker Myosin Heavy Chain (Mhc) by immunostaining (Fig. 7a and b and ESI Fig. 2†). Cryogels with EPS applied had a higher fusion index ($51.84 \pm 5.30\%$) in comparison with non-EPS stimulation ($25.54 \pm 5.06\%$) (Fig. 7c), indicating that the electrically stimulated cryogel enhanced the fusion of the cells into myotubes.[56,67,68] We performed a complementary study on the gene expression of some myogenic markers by qPCR to further analyze the effect of EPS in myogenic maturation. We selected three genes whose dynamic expressions would change during the muscle maturation: myogenin (Myog), myosin heavy chain 2 (Myh2) and troponin T1 (Tnnt1) (Fig. 7d–f). Myog is a marker that is expressed in the early maturation steps, when the myotubes are fusing. By gene amplification, we could observe that myogenin was still expressed in the EPS(+) cryogels. These results are in correlation with the obtained fusion index results. We observed that the cells started the myogenic differentiation as the myotubes were formed. However, this
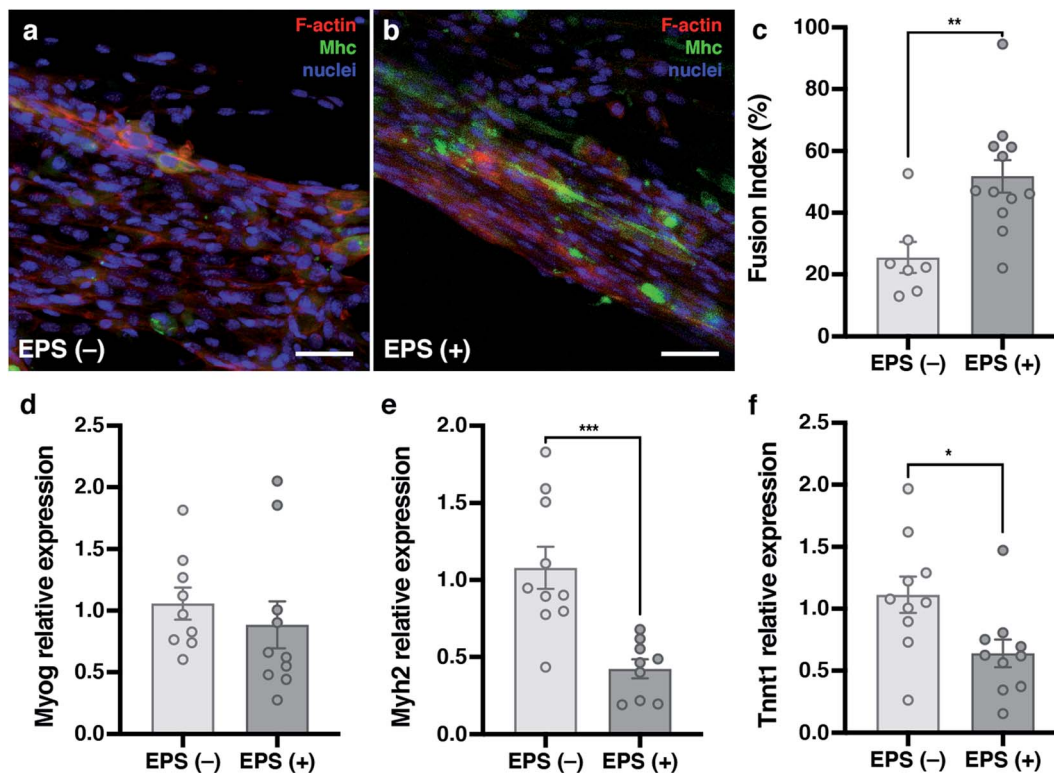
Fig. 7   Electrical Pulse Stimulation (EPS) enhances myogenic maturation. (a and b) Confocal merged images showing cells marked with phalloidin in red, cell nuclei counterstained in blue with DAPI and Mhc marked with Alexa-488 in green. Scale bars = 100 μm. (c) Graphs showing fusion index of CNTs(−) cryogels in light grey and CNTs(+) cryogels in dark grey. (d−f) Graphs of myogenic maturation marker expression. EPS(−) in light grey and EPS(+) in dark grey. (d) Myogenin. (e) Myosin heavy chain 2. (f) Troponin T1. Results are mean ± SEM. *p-value = 0.05.

might indicate that they were still in an early phase of the maturation. To confirm our hypothesis, we also analyzed both Myh2 and Tnnt1, which are late maturation markers. These markers are expressed when the tissue is fully mature. However, in our assay, these markers from a later myotube differentiation were downregulated, confirming that most myotubes in EPS(+) were in the first steps of the maturation process. Although we did not detect an increase of the late maturation markers by qPCR, we showed that the myotubes were formed and expressed Mhc (Fig. 7a and b). Moreover, the fusion index was higher in the EPS(+) cryogels and Myog was still expressed, meaning that the maturation process of the tissue already started. Taking this point as a mature step, we can conclude that our scaffold enhanced the cell maturation when EPS was applied. However, more research would be necessary to further enhance the myotube maturation.

Conclusion

Here, we present a new methodology to fabricate volumetric scaffolds to generate skeletal muscle *in vitro*. The technique used allows us to control not only the external morphology of the scaffold, but also the internal pore morphology and size in a highly controlled way. Our protocol shows a micro-porosity range scaffold with highly aligned fibers. In addition, its mechanical properties match well with the needs to engineer

skeletal muscle. Moreover, the addition of CNT to our scaffold has enhanced its electrical properties. All of this is possible without the loss of any other important properties of the scaffold to generate volumetrically larger skeletal muscle tissue. Herein, we proved that these composite scaffolds with integrated CNT are non-toxic, as the cells were viable, and enhanced the fusion of the cells due to its high alignment. Once the cells fused, taking advantages of the improved electrical properties of our doped-biomaterial scaffold, we could stimulate the cells. We proved that they could mature faster and better. In conclusion, our protocol shows a new doped-biomaterial composite scaffold that enhances the fusion and maturation of the cells by applying EPS, leading to a complete skeletal muscle generated *in vitro* with strong possibilities in tissue engineering, organ-on-a-chip technology or drug screening.

Conflicts of interest

There are no conflicts to declare.

Acknowledgements

References

1 S. Ahadian, J. Ramón-Azcón, S. Ostrovidov, G. Camci-Unal, V. Hosseini, H. Kaji, K. Ino, H. Shiku, A. Khademhosseini and T. Matsue, *Lab Chip*, 2012, **12**, 3491–3503.

2 M. Estili, A. Kawasaki and Y. Sakka, *Adv. Mater.*, 2012, **24**, 4322–4326.

3 S. Ahadian, J. Ramón-Azcón, S. Ostrovidov, G. Camci-Unal, H. Kaji, K. Ino, H. Shiku, A. Khademhosseini and T. Matsue, *Biomed. Microdevices*, 2013, **15**, 109–115.

4 T. D. Schmittgen and K. J. Livak, *Nat. Protoc.*, 2008, **3**, 1101–1108.

5 Y. A. Kim, T. Hayashi, M. Endo, Y. Kaburagi, T. Tsukada, J. Shan, K. Osato and S. Tsuruoka, *Carbon*, 2005, **43**, 2243–2250.

6 M. L. P. Langelaan, K. J. M. Boonen, K. Y. Rosaria-Chak, D. W. J. van der Schaft, M. J. Post and F. P. T. Baaijens, *J. Tissue Eng. Regener. Med.*, 2011, **5**, 529–539.

7 P. Zorlutuna, N. Annabi, G. Camci-Unal, M. Nikkhah, J. M. Cha, J. W. Nichol, A. Manbachi, H. Bae, S. Chen and A. Khademhosseini, *Adv. Mater.*, 2012, **24**, 1782–1804.

8 R. Gauvin and A. Khademhosseini, *ACS Nano*, 2011, **5**, 4258–4264.

9 M. Estili and A. Kawasaki, *Adv. Mater.*, 2010, **22**, 607–610.

10 M. Estili, A. Kawasaki, H. Sakamoto, Y. Mekuchi, M. Kuno and T. Tsukada, *Acta Mater.*, 2008, **56**, 4070–4079.

11 H. Aubin, J. W. Nichol, C. B. Hutson, H. Bae, A. L. Sieminski, D. M. Cropek, P. Akhyari and A. Khademhosseini, *Biomaterials*, 2010, **31**, 6941–6951.

12 D. Wang, S. Fujinami, H. Liu, K. Nakajima and T. Nishi, *Macromolecules*, 2010, **43**, 9049–9055.

13 H. Liu, N. Chen, S. Fujinami, D. Louzguine-Luzgin, K. Nakajima and T. Nishi, *Macromolecules*, 2012, **45**, 8770–8779.

14 B. Derjaguin, V. Muller and Y. Toporov, *J. Colloid Interface Sci.*, 1975, **53**, 314–326.

15 J. Ramon-Azcon, S. Ahadian, R. Obregon, G. Camci-Unal, S. Ostrovidov, V. Hosseini, H. Kaji, K. Ino, H. Shiku, A. Khademhosseini and T. Matsue, *Lab Chip*, 2012, **12**, 2959–2969.

16 H.-W. Kang, S. J. Lee, I. K. Ko, C. Kengla, J. J. Yoo and A. Atala, *Nat. Biotechnol.*, 2016, **34**, 312–319.

17 S. Ostrovidov, S. Salehi, M. Costantini, K. Suthiwanich, M. Ebrahimi, R. B. Sadeghian, T. Fujie, X. Shi, S. Cannata, C. Gargioli, A. Tamayol, M. R. Dokmeci, G. Orive, W. Swieszkowski and A. Khademhosseini, *Small*, 2019, **15**, 1805530.

18 A. García-Lizarribar, X. Fernández-Garibay, F. Velasco-Mallorquí, A. G. Castaño, J. Samitier and J. Ramon-Azcon, *Macromol. Biosci.*, 2018, **18**, 1–13.

19 M. A. Ortega, X. Fernández-Garibay, A. G. Castaño, F. De Chiara, A. Hernández-Albors, J. Balaguer-Trias and J. Ramón-Azcón, *Lab Chip*, 2019, **19**, 2568–2580.

20 W. Bian and N. Bursac, *Biomaterials*, 2009, **30**, 1401–1412.

21 Y. Morimoto, M. Kato-Negishi, H. Onoe and S. Takeuchi, *Biomaterials*, 2013, **34**, 9413–9419.

22 K. H. Nakayama, M. Shayan and N. F. Huang, *Adv. Healthcare Mater.*, 2019, 1801168.

23 L. Y. Jiang and Y. Luo, *Soft Matter*, 2013, **9**, 1113–1121.

24 M. Nikkhah, F. Edalat, S. Manoucheri and A. Khademhosseini, *Biomaterials*, 2012, **33**, 5230–5246.

25 R. Obregón, J. Ramón-Azcón, S. Ahadian, H. Shikul, H. Bae, M. Ramalingam and T. Matsue, *J. Nanosci. Nanotechnol.*, 2014, **14**, 487–500.

26 E. Engel, A. Michiardi, M. Navarro, D. Lacroix and J. A. Planell, *Trends Biotechnol.*, 2008, **26**, 39–47.

27 W. H. Ryu, R. J. Fasching, M. Vyakarnam, R. S. Greco and F. B. Prinz, *J. Microelectromech. Syst.*, 2006, **15**, 1457–1465.

28 A. E. Jakus, E. B. Secor, A. L. Rutz, S. W. Jordan, M. C. Hersam and R. N. Shah, *ACS Nano*, 2015, **9**, 4636–4648.

29 J.-O. You, M. Rafat, G. J. C. Ye and D. T. Auguste, *Nano Lett.*, 2011, **11**, 3643–3648.

30 H.-L. Tan, S.-Y. Teow and J. Pushpamalar, *Bioengineering*, 2019, **6**, 17.

31 V. Bonfrate, D. Manno, A. Serra, L. Salvatore, A. Sannino, A. Buccolieri, T. Serra and G. Giancane, *J. Colloid Interface Sci.*, 2017, **501**, 185–191.

32 S. Ahadian, J. Ramón-Azcón, M. Estili, X. Liang, S. Ostrovidov, H. Shiku, M. Ramalingam, K. Nakajima, Y. Sakka, H. Bae, T. Matsue and A. Khademhosseini, *Sci. Rep.*, 2015, **4**, 4271.

33 S. R. Shin, H. Bae, J. M. Cha, J. Y. Mun, Y.-C. Chen, H. Tekin, H. Shin, S. Farshchi, M. R. Dokmeci, S. Tang and A. Khademhosseini, *ACS Nano*, 2012, **6**, 362–372.

34 X. Su, Q. Zhang, Q. Zhong, L. Liu, H. Gao, R. Meng and J. Yao, *Fibers Polym.*, 2016, **17**, 712–720.

35 P. B. Welzel, M. Grimmer, C. Renneberg, L. Naujox, S. Zschoche, U. Freudenberg and C. Werner, *Biomacromolecules*, 2012, **13**, 2349–2358.

36 A. Béduer, T. Braschler, O. Peric, G. E. Fantner, S. Mosser, P. C. Fraering, S. Benchérif, D. J. Mooney and P. Renaud, *Adv. Healthcare Mater.*, 2015, **4**, 301–312.

37 X. Wu, Y. Liu, X. Li, P. Wen, Y. Zhang, Y. Long, X. Wang, Y. Guo, F. Xing and J. Gao, *Acta Biomater.*, 2010, **6**, 1167–1177.

38 J. Wu, Q. Zhao, J. Sun and Q. Zhou, *Soft Matter*, 2012, **8**, 3620.

39 C. B. Hutson, J. W. Nichol, H. Aubin, H. Bae, S. Yamanlar, S. Al-Haque, S. T. Koshy and A. Khademhosseini, *Tissue Eng., Part A*, 2011, **17**, 1713–1723.

40 R. Reeves, A. Ribeiro, L. Lombardo, R. Boyer and J. B. Leach, *Polym*, 2012, **2**, 252–264.

41 É. Georget, R. Abdeddaim and P. Sabouroux, *C. R. Phys.*, 2014, **15**, 448–457.

42 D. Ba and P. Sabouroux, *Microw. Opt. Technol. Lett.*, 2010, **52**, 2643–2648.

43 A. L. Neves, E. Georget, N. Cochinaire and P. Sabouroux, *Rev. Sci. Instrum.*, 2017, **88**, 084706.

44 A. M. Nicolson and G. F. Ross, *IEEE Trans. Instrum. Meas.*, 1970, **19**, 377–382.

45 W. B. Weir, *Proc. IEEE*, 1974, **62**, 33–36.

46 A. García-Lizarribar, X. Fernández-Garibay, F. Velasco-Mallorquí, A. G. Castaño, J. Samitier and J. Ramon-Azcon, *Macromol. Biosci.*, 2018, **18**, 1800167.

47 R. Seyedmahmoud, B. Çelebi-Saltik, N. Barros, R. Nasiri, E. Banton, A. Shamloo, N. Ashammakhi, M. R. Dokmeci and S. Ahadian, *Micromachines*, 2019, **10**, 679.

48 V. Hosseini, S. Ahadian, S. Ostrovidov, G. Camci-Unal, S. Chen, H. Kaji, M. Ramalingam and A. Khademhosseini, *Tissue Eng., Part A*, 2012, **18**, 2453–2465.

49 P. Molnar, W. Wang, A. Natarajan, J. W. Rumsey and J. J. Hickman, in *Biotechnology Progress*, 2007, vol. 23, pp. 265–268.

50 A. Bettadapur, G. C. Suh, N. A. Geisse, E. R. Wang, C. Hua, H. A. Huber, A. A. Viscio, J. Y. Kim, J. B. Strickland and M. L. McCain, *Sci. Rep.*, 2016, **6**, 1–14.

51 A. J. Engler, M. A. Griffin, S. Sen, C. G. Bönnemann, H. L. Sweeney and D. E. Discher, *J. Cell Biol.*, 2004, **166**, 877–887.

52 C. Snyman, K. P. Goetsch, K. H. Myburgh and C. U. Niesler, *Front. Physiol.*, 2013, **4**, 349.

53 C. Monge, K. Ren, K. Berton, R. Guillot, D. Peyrade and C. Picart, *Tissue Eng., Part A*, 2012, **18**, 1664–1676.

54 N. F. Huang, R. J. Lee and S. Li, *Am. J. Transl. Res.*, 2010, **2**, 43–55.

55 N. Jiwlawat, E. M. Lynch, B. N. Napiwocki, A. Stempien, R. S. Ashton, T. J. Kamp, W. C. Crone and M. Suzuki, *Biotechnol. Bioeng.*, 2019, **116**, 2377–2392.

56 H. Park, R. Bhalla, R. Saigal, M. Radisic, N. Watson, R. Langer and G. Vunjak-Novakovic, *J. Tissue Eng. Regener. Med.*, 2008, **2**, 279–287.

57 S. Sirivisoot and B. S. Harrison, *Int. J. Nanomed.*, 2011, **6**, 2483–2497.

58 M. C. Chen, Y. C. Sun and Y. H. Chen, *Acta Biomater.*, 2013, **9**, 5562–5572.

59 M. Kharaziha, S. R. Shin, M. Nikkhah, S. N. Topkaya, N. Masoumi, N. Annabi, M. R. Dokmeci and A. Khademhosseini, *Biomaterials*, 2014, **35**, 7346–7354.

60 S. Romanazzo, G. Forte, M. Ebara, K. Uto, S. Pagliari, T. Aoyagi, E. Traversa and A. Taniguchi, *Sci. Technol. Adv. Mater.*, 2012, **13**, 064211.

61 N. Sachot, E. Engel and O. Castano, *Curr. Org. Chem.*, 2014, **18**, 2299–2314.

62 L. E. Bertassoni, M. Cecconi, V. Manoharan, M. Nikkhah, J. Hjortnaes, A. L. Cristino, G. Barabaschi, D. Demarchi, M. R. Dokmeci, Y. Yang and A. Khademhosseini, *Lab Chip*, 2014, **14**, 2202–2211.

63 A. S. Salimath and A. J. García, *J. Tissue Eng. Regener. Med.*, 2016, **10**, 967–976.

64 J. Ramón-Azcón, S. Ahadian, M. Estili, X. Liang, S. Ostrovidov, H. Kaji, H. Shiku, M. Ramalingam, K. Nakajima, Y. Sakka, A. Khademhosseini and T. Matsue, *Adv. Mater.*, 2013, **25**, 4028–4034.

65 J. Ren, Q. Xu, X. Chen, W. Li, K. Guo, Y. Zhao, Q. Wang, Z. Zhang, H. Peng and Y. G. Li, *Adv. Mater.*, 2017, **29**, 1–8.

66 H. Takahashi, T. Shimizu, M. Nakayama, M. Yamato and T. Okano, *Biomaterials*, 2013, **34**, 7372–7380.

67 A. Ito, Y. Yamamoto, M. Sato, K. Ikeda, M. Yamamoto, H. Fujita, E. Nagamori, Y. Kawabe and M. Kamihira, *Sci. Rep.*, 2015, **4**, 4781.

68 R. Banan Sadeghian, M. Ebrahimi and S. Salehi, *J. Tissue Eng. Regener. Med.*, 2018, **12**, 912–922.